Local charge measurement using off-axis electron holography

OPEN ACCESS
IOP Publishing
Journal of Physics D: Applied Physics
J. Phys. D: Appl. Phys. **49** (2016) 294003 (16pp)
doi:10.1088/0022-3727/49/29/294003

Local charge measurement using off-axis electron holography

M Beleggia[1], L C Gontard[2,3] and R E Dunin-Borkowski[4]

[1] Center for Electron Nanoscopy, Technical University of Denmark, DK-2800 Kgs. Lyngby, Denmark
[2] Department of Materials Science and Metallurgical Engineering and Inorganic Chemistry, Universidad de Cádiz, Puerto Real, Cadiz E-11510, Spain
[3] Servicio de Microscopía Centro de Investigación, Tecnología e Innovación (CITIUS), Universidad de Sevilla, Av. Reina Mercedes 4b, 41012 Sevilla, Spain
[4] Ernst Ruska-Centre for Microscopy and Spectroscopy with Electrons and Peter Grünberg Institute, Forschungszentrum Jülich, D-52425 Jülich, Germany

E-mail: mb@cen.dtu.dk

Received 21 March 2016, revised 3 May 2016
Accepted for publication 9 May 2016
Published 4 July 2016

Abstract

A model-independent approach based on Gauss' theorem for measuring the local charge in a specimen from an electron-optical phase image recorded using off-axis electron holography was recently proposed. Here, we show that such a charge measurement is reliable when it is applied to determine the total charge enclosed within an object. However, the situation is more complicated for a partial charge measurement when the integration domain encloses only part of the object. We analyze in detail the effects on charge measurement of the mean inner potential of the object, of the presence of induced charges on nearby supports/electrodes and of noise. We perform calculations for spherical particles and highlight the differences when dealing with other object shapes. Our analysis is tested using numerical simulations and applied to the interpretation of an experimental dataset recorded from a sapphire particle.

Keywords: electron holography, electrostatics, dielectric nanoparticles, charge measurement, electrostatic potential

(Some figures may appear in colour only in the online journal)

1. Introduction

Off-axis electron holography is a powerful technique for measuring projected electrostatic potentials in materials in the transmission electron microscope (TEM) [1–5]. It makes use of the superposition of an object wave and a reference wave to form an interference pattern in the image plane, from which the phase of the object electron wavefunction can be recovered. For a non-magnetic material, in the absence of dynamical diffraction the phase recorded using off-axis electron holography can be written in the form

$$\varphi(x, y) = C_{\mathrm{E}} \int_{-\infty}^{+\infty} V_{\mathrm{tot}}(x, y, z)\mathrm{d}z, \qquad (1)$$

where z is the incident electron beam direction, V_{tot} is the total electrostatic potential within and around the specimen (including contributions from both charge distributions and the mean inner potential) and C_{E} is a constant that depends on the microscope accelerating voltage.

However, information about how charges (i.e. field sources) are distributed within the specimen is often more valuable than a measurement of the projected electrostatic potential, as the distribution of charges reflects the response of the object to an external stimulus and boundary conditions. Furthermore, once the distribution of field sources is known, the electrostatic potential or field can then be computed straightforwardly, while the reverse approach requires solving an inverse problem.

The mapping of electrostatic potentials using off-axis electron holography has a long history [6, 7]. The technique has been successfully applied to study semiconductor p-n junctions [8–11], recently also in three dimensions [12, 13], electron

beam induced charging of TEM specimens [14–18], mean inner potentials of materials [19–21], electrically biased carbon nanotubes [22, 23], electrically biased metallic needles [24–27], electron beam induced potentials [28] and the electrostatic Aharonov–Bohm effect [29]. For a recent review, see [30].

Many of these studies approach the interpretation of the measured projected electrostatic potential by fitting a recorded phase image to a model that depends on a number of unknown free parameters, including electron-optical parameters (the interference distance, accelerating voltage, position of the sample in the column, illumination characteristics, etc), geometrical parameters (the shape of the object, presence or absence of a support, distance to a grounded electrode, etc) and physical parameters (the properties of the material, temperature, environment, etc). The result of using such a fitting procedure is assumed to be representative of the true projected electrostatic potential within and around the object, subject to a given set of boundary conditions. However, the reliability of the result is as representative of reality as the model is and the solution is not necessarily unique as a result of the large number of free parameters involved. It is also the case that good models are often only available for simple geometries and basic responses (e.g. linear dielectric, ideal metal, etc). For most samples, a physical model that can be used to interpret a phase image simply does not exist, even for a relatively simple geometry such as a thin-film p-n junction with an unknown surface state, either because its construction requires the very same knowledge that needs to be determined from the experimental measurement or because the numerical tools that are required (e.g. finite element methods) produce only one model at a time, corresponding to a single point in a multi-dimensional parameter space.

Even if a perfect model that provides a best fit to a phase image can be found, it usually provides only a single projection of a three-dimensional electrostatic potential. Although electron holographic tomography is becoming a viable option for obtaining three-dimensional information about electrostatic potentials experimentally [31, 32] and although it is associated with additional technical challenges (e.g. missing wedge, alignment issues, diffraction contrast and stability of the charge state in the object with tilt angle and time), it does not require fitting of the data and therefore qualifies as a model-independent approach for measuring electrostatic potentials in three dimensions.

The ultimate goal, however, is the determination of field sources, i.e. charge distributions, in order to understand how a material reacts to a given external stimulus, how it polarizes under the influence of an electric field, how much charge is transferred from one object to another as a result of an electrochemical potential difference, how many dopants are active in a semiconductor, where do ions and charge carriers accumulate or deplete, why these phenomena happen and how they evolve and can be controlled. The target of any *ab initio* calculation of a material or structure is its charge density and the potential is considered as a 'by-product', which combines charge density and geometry in a way that can mask the underlying information. For example, as any radially symmetrical charge density that is associated with total charge Q, regardless of its functional form, produces the same Coulomb electric field in the space surrounding the charged object, the determination of how Q is distributed within the object based on a knowledge of the vacuum potential alone is impossible. Similarly, the far field of any charged object loses any dependence on its dielectric characteristics, as these are solely responsible for the internal charge redistribution effected by self-polarization screening and never affect the total amount of charge that is present.

The determination of the local charge distribution is, therefore, essential in order to disentangle the complex interplay between physics, geometry and external stimuli and to understand the link between structure and functionality of nanostructures in a quantitative fashion. Here, we discuss the reliability of charge measurements carried out using a recently proposed model-independent scheme based on the Gauss theorem [23]. We address partial charge measurements, for which the integration domain encloses only part of the object. We identify the combined influence of variations in mean inner potential and specimen thickness as the main source of artefacts and consider the influence of noise and finite spatial resolution. We perform calculations for spherical particles and highlight differences when dealing with other three-dimensional object shapes. Finally, we test our analysis using numerical simulations and apply it to the interpretation of an experimental dataset recorded from a sapphire particle.

It should be noted that the primary focus of this paper is the analysis of phase images recorded using the off-axis mode of electron holography in the TEM. However, our conclusions are equally applicable to phase images retrieved using other approaches, such as ptychography [33] or the application of the transport of intensity equation to a defocus series of bright-field images [34, 35], as well as to the interpretation of phase gradient images recorded using techniques such as Foucault imaging [36, 37] and differential phase contrast imaging in the scanning TEM [38–40].

2. Electrostatics of charged dielectrics

We begin by considering a point charge Q located at $\mathbf{r} = \mathbf{r}_0$ within a linear dielectric object of relative dielectric constant $\epsilon_r = \epsilon/\epsilon_0$. Inside the object, the potential V that results from the presence of the charge satisfies Poisson's equation

$$\nabla^2 V = -\frac{\rho}{\epsilon} = -\frac{Q}{\epsilon}\delta^3(\mathbf{r} - \mathbf{r}_0), \tag{2}$$

while outside the object the potential satisfies Laplace's equation $\nabla^2 V = 0$. The interior and exterior solutions are connected by standard boundary conditions (continuity of the perpendicular component of $\mathbf{D}$ and of the tangential component of $\mathbf{E}$) across the object's surface.

Poisson's equation (equation (2)), with ϵ in the denominator, is valid only for a linear dielectric for which $\mathbf{P} = \epsilon_0\chi\mathbf{E}$, where $\chi = \epsilon_r - 1$ is the dielectric susceptibility. In fact,

$$\nabla^2 V = -\frac{\rho_{\text{tot}}}{\epsilon_0} = -\frac{\rho + \rho_{\text{pol}}}{\epsilon_0} = -\frac{\rho - \nabla\cdot\mathbf{P}}{\epsilon_0}. \tag{3}$$

Hence,

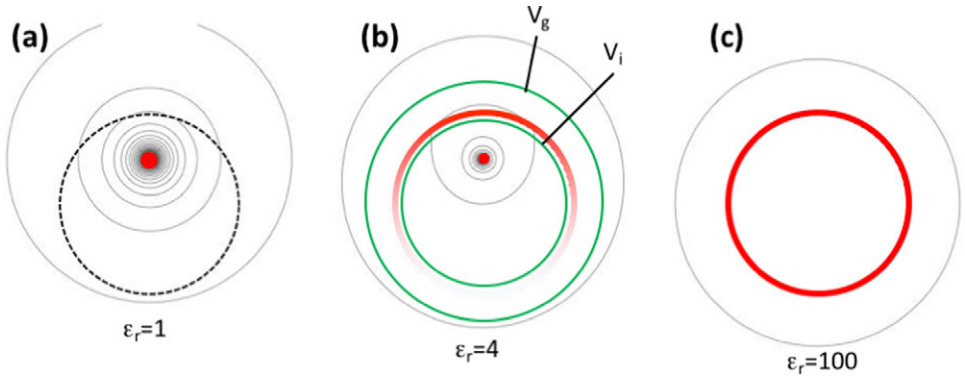

Figure 1. Schematic diagrams showing equipotential contours (thin black lines) for a point charge located in a spherical object whose relative dielectric constant ϵ_r is (a) 1, (b) 4 and (c) 100. The boundary of the object is marked by a dashed black line in (a). In each diagram, the charge density in the object is shown in red. The green lines and symbols in (b) mark Gaussian volumes (see text for details).

$$-\nabla\cdot\mathbf{P} = -\epsilon_0\chi\nabla\cdot\mathbf{E} = \epsilon_0\chi\nabla^2 V \tag{4}$$

and

$$\nabla^2 V(1+\chi) = -\frac{\rho}{\epsilon_0}, \tag{5}$$

which is equation (2). The derivation leading to equation (5) illustrates how the dielectric constant ϵ captures the polarization response of the object to the point charge.

At the object's surface, where it has an interface with vacuum, surface polarization charges $\sigma_{\mathrm{pol}} = \mathbf{P}\cdot\hat{\mathbf{n}}$ arise, so that a portion of the charge Q appears as if it were transferred to the surface, thereby affecting the potential in both the interior and the exterior region. Since polarization is simply charge displacement, the total charge in the object always remains Q, regardless of the value of ϵ_r. However, its distribution changes, such that the point charge Q located in the object's interior appears to decrease to Q/ϵ_r and the remaining fraction $(1-1/\epsilon_r)$ is effectively brought to the object's surface.

This situation is described in figure 1, in which equipotential contours have been sketched for a point charge located in a spherical object whose relative dielectric constant ϵ_r is (a) 1, (b) 4 or (c) 100. Note that the potential in (a) is identical to that of a point charge in vacuum, since an object for which $\epsilon_r = 1$ does not polarize. The potential in figure 1(c) is identical to that generated by a uniform charge distribution on the surface of the object and the interior is at a constant potential of $Q/(4\pi\epsilon_0 R)$, where R is the radius of the sphere. When the dielectric constant is very large, the object therefore behaves as a metal, with any charge added to the interior being transported to the surface. The surface (as well as the whole object) then becomes an equipotential. In the intermediate case shown in figure 1(b), the surface becomes charged, but the charge distribution on the surface is in general non-uniform, so that the object is not equipotential and both the interior and the exterior field retain an impression of the location of the charge.

In order to further illustrate this concept, Gauss' law can be applied to a Gaussian volume V_g that encloses the entire dielectric object. Such a Gaussian volume is represented by the larger green contour in figure 1(b). Then,

$$-\int_{V_g}\nabla^2 V\,\mathrm{d}V_g = \int_{V_g}\nabla\cdot\mathbf{E}\,\mathrm{d}V_g = \int_{S_g}\mathbf{E}\cdot\hat{\mathbf{n}}\,\mathrm{d}S_g = \frac{Q}{\epsilon_0}, \tag{6}$$

independent of the location $\mathbf{r}_0$ of the charge and of the dielectric constant. If, however, the Gaussian volume V_g is split into an interior part V_i (smaller green contour in figure 1(b) where the potential satisfies Poisson's equation (equation (2))) and an exterior part V_e where the potential satisfies Laplace's equation and equation (2) is inserted directly into (6), then only the fraction of charge that has remained in the interior is captured:

$$-\int_{V_g}\nabla^2 V\,\mathrm{d}V_g = -\int_{V_i}\nabla^2 V\,\mathrm{d}V_i = \frac{Q}{\epsilon}\int_{V_i}\delta^3(\mathbf{r}-\mathbf{r}_0)\,\mathrm{d}V_i = \frac{Q}{\epsilon}. \tag{7}$$

The fraction $(1-1/\epsilon_r)$ of charge that is effectively moved to the surface is then missed. This statement is independent of the object's shape. However, the shape of the object determines how the charge is distributed on its surface.

3. Total charge measurement

In the absence of dynamical diffraction, a phase image retrieved from an off-axis electron hologram of a non-magnetic charged dielectric object is proportional to the total electrostatic potential $V_{\mathrm{tot}} = V + V_{\mathrm{M}}$ projected in the electron beam direction according to the expression

$$\varphi(x,y) = C_{\mathrm{E}}\int_{-\infty}^{+\infty} V(x,y,z)\mathrm{d}z + C_{\mathrm{E}}V_{\mathrm{M}}t_p(x,y), \tag{8}$$

where V_{M} is the mean inner potential (MIP) of the object, $t_p(x, y)$ is its projected thickness and the potential $V(x, y, z)$ is related to the unknown charge distribution in the sample by Poisson's equation

$$\nabla^2 V = -\frac{\rho_{\mathrm{tot}}}{\epsilon_0}. \tag{9}$$

In equation (9), ρ_{tot} includes *all* of the physical charges that are present, including charges that have been added to the object (the quantity of primary interest), volume and surface polarization charges and, if applicable, induced (bound and/or mobile) charges on, e.g. the part of the support film that lies within the field of view.

The application of a two-dimensional Laplacian operator $\nabla_2^2 = \partial_x^2 + \partial_y^2 = \nabla^2 - \partial_z^2$ to the phase image then gives

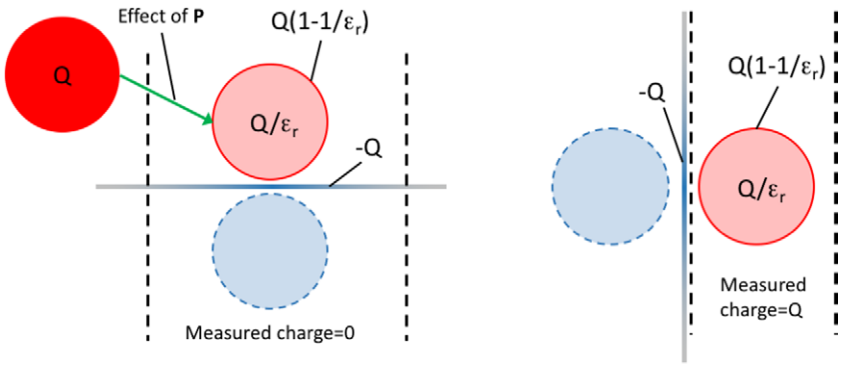

Figure 2. Schematic diagrams showing a spherical dielectric particle supported by a conducting substrate that is kept at ground potential. The support, whose surface is indicated by the thick grey line, is located either underneath the object (left) or to one side of it (right). The electron beam direction is vertical. In the diagrams, red colouring denotes physical charges, while blue colouring indicates induced charges (fading thick blue line on the grounded plane) or their equivalent image charge distribution mirroring the physical charges (blue dashed lines and circles). The black dashed lines show the boundaries of the integration domain. (See text for details.)

$$\nabla_2^2\varphi(x,y) = -\frac{C_\mathrm{E}}{\epsilon_0}\sigma_p(x,y) + C_\mathrm{E}V_\mathrm{M}\nabla_2^2 t_p(x,y), \tag{10}$$

where

$$\sigma_p(x,y) = \int_{-\infty}^{+\infty} \rho_\mathrm{tot}(x,y,z)\mathrm{d}z \tag{11}$$

is the projected total charge distribution. In deriving equation (10), the term arising from the $-\partial_z^2$ derivative

$$-C_\mathrm{E}\int_{-\infty}^{+\infty} \partial_z^2 V(x,y,z)\mathrm{d}z = -C_\mathrm{E}\partial_z V(x,y,z)\Big|_{z=-\infty}^{z=+\infty} \tag{12}$$

disappears because the electric field generated by any localized charge distribution (i.e. one that does not extend to infinity) vanishes at infinity.

By integrating the Laplacian of the phase over a surface S that encloses the entire object, which is initially imagined to be floating in vacuum, the charge Q is retrieved precisely through the relation

$$\int_S \nabla_2^2\varphi(x,y)\mathrm{d}x\mathrm{d}y = -\frac{C_\mathrm{E}}{\epsilon_0}Q \tag{13}$$

because neither the MIP term nor the polarization charge distribution bear a net charge. Since $\nabla_2^2\varphi = \nabla_2\cdot\nabla_2\varphi$ by virtue of the two-dimensional Green's theorem

$$\int_S \nabla_2^2\varphi\mathrm{d}S = \oint_\ell \nabla_2\varphi\cdot\hat{\mathbf{n}}\,\mathrm{d}\ell, \tag{14}$$

the same total charge Q can be measured equivalently by contour integration of the phase gradient over the boundary ℓ of the chosen integration domain S (an approach adopted in [41]). As we discuss below, surface integration of the Laplacian of the phase and contour integration of the phase gradient perform identically with respect to the influence of noise on the measurement uncertainty—the two approaches are completely equivalent.

If the object is supported by a conducting substrate that is kept at ground potential, then the induced charge distribution on the support film will compensate the charge Q on the object exactly, yielding a null measurement of the charge if the support film is underneath the object. If, however the induced charges are displaced laterally, as may happen if the object protrudes from a vertical support that lies outside the integration domain, then the measurement yields the correct value of Q. These situations are sketched in figure 2 for a spherical dielectric particle that is charged uniformly (before considering the effect of the polarization) and supported either from underneath or laterally by a grounded conducting film.

3.1. Influence of the support on the charge density

In figure 2, a passive support whose role was mainly to provide a platform for induced charges to accumulate was considered. However, if an object is in the vicinity of a grounded electrode or in contact with it, the induced charge distribution will affect the charge density on the object as a result of image forces. The scenario of a charged metallic spherical particle approaching a grounded plane was explored in [42]. The analysis then revealed that the surface charge distribution, which is uniform at large distances from the grounded plane, evolved towards a state where charge accumulated at the pole closest to the electrode. The potential of the sphere decreased logarithmically to zero upon contact. All of the charge then condensed to a point that overlapped with the induced charge, which also decreased to a point. A similar scenario will occur in the case of a dielectric particle that has a finite value of ϵ_r, although only the polarization charges will rearrange themselves over the surface, while the underlying charge distribution will remain frozen in place if the material is a perfect insulator.

By adopting the same computational framework as in [42], the effect on the charge distribution in a dielectric sphere of its proximity to a grounded plane can be assessed. We consider two dielectric spheres with $\epsilon_r = 10$ and $\epsilon_r = 3$ displaced from a grounded plane by half their radius. When the object is isolated, as shown in figures 3(a) and (g), we expect the unperturbed charge configuration with a fraction $1/\epsilon_r$ of charge uniformly distributed through the volume, and the remaining fraction uniformly distributed through the surface. The resulting potential distribution, shown in figures 3(d) and (j), confirms that the surface is equipotential (black lines in figures 3(d) and (j)), and the surface charge density uniform

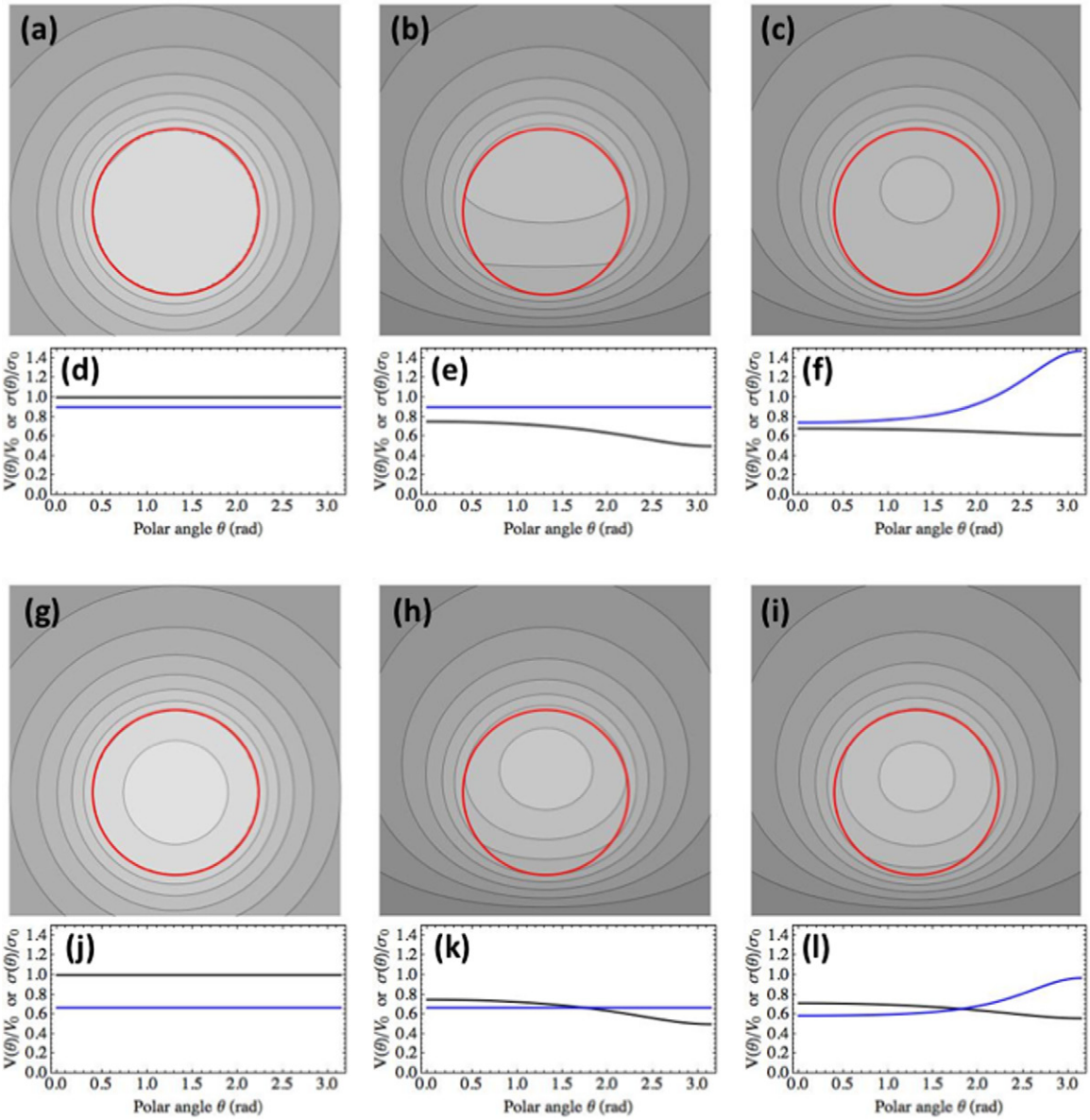

Figure 3. Calculations of the effect on the charge distribution on a dielectric sphere of its proximity to a grounded plane located at the bottom edge of ((b), (c)) and ((h), (i)). Top ((a)–(f)): dielectric sphere with $\epsilon_r = 10$; bottom ((g)–(l)): dielectric sphere with $\epsilon_r = 3$. From left to right: isolated object (no support), passive support, active support. Equipotential contours in ((a)–(c)) and ((g)–(i)) are drawn at 0.1 V/V_0 intervals on a meridian section of the sphere, where $V_0 = Q/(4\pi\epsilon_0 R)$, Q is the amount of net charge on the sphere, and R is the sphere radius. Profiles in ((d)–(f)) and ((j)–(l)) are taken along any of the spheres' meridians, and indicate potential (black) and surface charge density (blue) from the north pole $\theta = 0$ to the south pole $\theta = \pi$. The surface charge density curves are normalized to $\sigma_0 = Q/(4\pi R^2)$.

(blue lines in figures 3(d) and (j)). The profiles are taken as a function of the polar angle θ, which corresponds to any of the spheres' meridians. However, the potential inside the objects is not constant, as indicated by the presence of internal equipotential contours. The presence of a 'passive' grounded plane with induced charges results in the potential distributions shown in figures 3(b) and (h), which now vary also over the surface of the objects, as shown in figures 3(e) and (k) (black curves), without, however, affecting the charge distribution of the object, as shown in figures 3(e) and (k) (blue lines). If the support becomes 'active', so that charges are allowed to relax, then the induced charges will polarize the region near the south pole of the spheres more than the rest of the object, due to proximity. The surface then develops a dipole term, with the upper hemisphere less positively charged than the bottom half. In turns, this changes the induced charge distribution, which will be more concentrated beneath the object. Relaxation continues until an equilibrium is found between all the multipole terms involved. The calculations shown in figure 3 required 20 multipoles. Once charges settle, we find that the surface charge distribution is non-uniform, with accumulation of charge at the south pole as shown in figures 3(f) and (l) (blue curves) and a residual potential variation along the meridians, figures 3(f) and (l) (black curves), which is allowed by the assumed insulating behavior of the objects. The integrated charge density is always equal to the expected amount $(1 - 1/\epsilon_r)$, indicating that there is no transfer of net charge between the bulk and the surface. The relative similarity of the potential contours shown

in figure 3 illustrates how difficult it is, in general, to draw conclusions about surface charge distributions directly from maps of (projected) potential. Figure 3 highlights once more the fact that materials with large dielectric constants behave effectively as metals, with charge distributions that evolve so as to make the body, as well as its surface, equipotential.

4. Partial charge measurement using electron holography

If the chosen integration domain S does not enclose the entire object, then an attempt to measure the charge generally differs from the true amount of charge that is physically present within the fraction of the object that is enclosed by S. This discrepancy results from the combined effects of the MIP contribution to the phase shift and induced charges on the supporting film (if one is present). We consider these contributions separately, focusing on a uniformly charged sphere for illustrative purposes.

4.1. Effective charge density of a uniformly charged dielectric sphere

When charge Q is distributed uniformly throughout the volume of a sphere of radius R, polarization effectively lowers the volume charge density by a factor $1/\epsilon_r$ and brings the remaining fraction of the charge to the surface. In the presence of a grounded conducting substrate, induced charges will be attracted onto the substrate, resulting in a planar surface charge distribution adjacent to the object.

As discussed above, the induced charges are also responsible for polarizing the dielectric. However, in order to avoid excessive complexity, here we consider only a 'passive' support, as previously defined.

Furthermore, the step in MIP at the object's surface corresponds to an additional effective charge distribution that can be treated as a dipole layer [43, 44].

Therefore, the total charge density that an electron effectively encounters when crossing a charged sphere is

$$\rho(r) = \frac{\rho_0}{\epsilon_r}\Theta(R-r) + \sigma_0\left(1-\frac{1}{\epsilon_r}\right)\delta(r-R) + \sigma_i(r_\perp)\delta(z) - \epsilon_0 V_{\mathrm{M}}\nabla^2\Theta(R-r), \tag{15}$$

where $\rho_0 = 3Q/(4\pi R^3)$ is the volume charge density that results from distributing Q throughout the volume of the sphere, $\sigma_0 = Q/(4\pi R^2)$ is the surface charge density that results from distributing Q through the surface of the sphere, $r_\perp = \sqrt{x^2+y^2}$ is the modulus of the projection of the position vector $\mathbf{r}$ onto the $z=0$ plane, $\Theta(x)$ is Heaviside's theta function, equal to 1 when $x>0$ and equal to 0 when $x<0$, and $\delta(x)$ is the Dirac delta distribution. The two functions $\Theta(x)$ and $\delta(x)$ are connected by a distributional derivative: $\mathrm{d}\Theta(x)/\mathrm{d}x = \delta(x)$. In equation (15), the first term indicates the volume charge density reduced by the dielectric constant, the second term captures the fraction of charge brought to the surface by the polarization, the third term describes the induced planar charge density that develops at the surface of the grounded support, and the last term represents the effective charge density associated with the MIP potential step across the object's interface with vacuum.

Since the external potential of a radially symmetrical charge distribution that bears a net charge Q is always a pure Coulomb potential and the MIP is confined to the object, the induced charge distribution can be calculated simply by using a single point image charge located a distance of one radius below the grounded plane (located at $z=-R$), if the support is considered passive and the sphere is touching it. The potential of the image charge is then $-Q/(4\pi\epsilon_0\sqrt{r_\perp^2+(z+2R)^2})$, so that the discontinuity of the electric field at the ground plane $\Delta E_z = \sigma_i/\epsilon_0$ is

$$-\frac{Q}{4\pi\epsilon_0}\frac{\partial}{\partial z}\left(\frac{1}{\sqrt{r_\perp^2+z^2}} - \frac{1}{\sqrt{r_\perp^2+(z+2R)^2}}\right)\Bigg|_{z=-R}. \tag{16}$$

Therefore:

$$\sigma_i(r_\perp) = -\frac{2\sigma_0}{(1+(r_\perp/R)^2)^{3/2}}. \tag{17}$$

The last term in equation (15), representing the effective charge distribution associated with the MIP, can be expressed formally as

$$-\epsilon_0 V_{\mathrm{M}}\nabla^2\Theta(R-r) = \sigma_{\mathrm{M}}\delta(r-R) + \frac{\sigma_{\mathrm{M}}R}{2}\delta'(r-R), \tag{18}$$

which stems from the curvature of the object, and can be interpreted as an additional *positively* charged spherical shell ($\sigma_{\mathrm{M}} = 2\epsilon_0 V_{\mathrm{M}}/R$ is positive since V_{M} is positive) enclosed within a spherical dipole layer, which can be imagined as a spherical capacitor with an infinitesimal gap. The derivative of the Dirac delta can be imagined as two oppositely charged spherical shells separated by an infinitesimal distance h, according to the expression

$$\frac{\sigma_{\mathrm{M}}R}{2}\delta'(r-R) = \lim_{h\to 0}\frac{\sigma_{\mathrm{M}}R}{2h}(\delta(r-R) - \delta(r-(R+h))). \tag{19}$$

The charge density on the two 'electrodes' of this spherical capacitor naturally diverges as $h\to 0$, since $1/h$ is a measure of its capacitance per unit area.

The fact that the total charge on the sphere remains Q and is compensated by $-Q$ on the support film can be verified explicitly by integrating $\rho(r)$ throughout space. Then:

$$4\pi\int_0^\infty r^2\mathrm{d}r\rho(r) = \frac{Q}{\epsilon_r} + Q\left(1-\frac{1}{\epsilon_r}\right) + Q_{\mathrm{M}} - Q_{\mathrm{M}} - Q = 0 \tag{20}$$

since

$$4\pi\rho_0\int_0^\infty r^2\mathrm{d}r\Theta(R-r) = 4\pi\rho_0\int_0^R r^2\mathrm{d}r = Q \tag{21}$$

$$4\pi\sigma_0\int_0^\infty r^2\mathrm{d}r\delta(r-R) = Q \tag{22}$$

$$4\pi\sigma_{\mathrm{M}}\int_0^\infty r^2\mathrm{d}r\delta(r-R)=4\pi R^2\sigma_{\mathrm{M}}=8\pi\epsilon_0 V_{\mathrm{M}}R=Q_{\mathrm{M}} \tag{23}$$

$$2\pi\sigma_{\mathrm{M}}R\int_0^\infty r^2\mathrm{d}r\delta'(r-R)=-Q_{\mathrm{M}} \tag{24}$$

$$4\pi\sigma_0\int_{-\infty}^{+\infty}\mathrm{d}z\int_0^\infty r_\perp\mathrm{d}r_\perp\frac{\delta(z)}{(1+(r_\perp/R)^2)^{3/2}}=Q. \tag{25}$$

Equation (24) is obtained by using the definitory property of $\delta'(x)$, i.e.

$$\int\delta'(x)f(x)\mathrm{d}x=-f'(0) \tag{26}$$

and suggests that the dipole layer that $\delta'(x)$ represents is not, by itself, charge neutral. This is because the outer 'electrode' is slightly larger than the inner 'electrode' and therefore carries more charge. By using equation (19) once more, we find that the inner layer has an amount of charge

$$Q_{\mathrm{M}}\lim_{h\to0}\frac{R}{2h}, \tag{27}$$

while the outer layer has an amount of charge

$$-Q_{\mathrm{M}}\lim_{h\to0}\left(1+\frac{R}{2h}\right), \tag{28}$$

illustrating how the outer negative layer compensates both the finite layer of positive charge resulting from the curvature of the object (equation (23)) and the divergent amount of charge present in the inner positive layer.

The resulting picture of the total effective charge density is sketched in figure 4. Although the drawing is not to scale, it reflects the relative magnitudes of the charges that are involved. In general, even the apparent charge Q_{M} resulting from the object's curvature can be much larger than the typical amount of charge that is embedded in a small dielectric nanoparticle. For example, a value for V_{M} of 15 V effectively corresponds to an amount Q_{M} of approximately 2000 e of positive charge on the (inner) surface of a sphere with $R=100$ nm. If the same amount of charge were to be physically deposited on the same spherical surface, it would result in a surface potential of $2V_{\mathrm{M}}=30$ V, which seems unlikely.

4.2. The resulting effective projected charge density

Projecting the volume charge term in $\rho(r)$ leads to

$$\frac{\rho_0}{\epsilon_r}t_p(r)\Theta(R-r), \tag{29}$$

where $t_p(r)=2\sqrt{R^2-r^2}$ (dropping the $\perp$ subscript on r for ease of notation, so that from now on $r=\sqrt{x^2+y^2}$) is the projected thickness of a spherical particle. Projection of the induced charge distribution just drops its $\delta(z)$ and leaves $\sigma_i(r)$ unaltered. Projection of a spherical shell of radius R with charge density $\sigma_{\mathrm{pol}}=\sigma_0(1-1/\epsilon_r)$ gives

$$\frac{4\sigma_{\mathrm{pol}}R}{t_p(r)}\Theta(R-r). \tag{30}$$

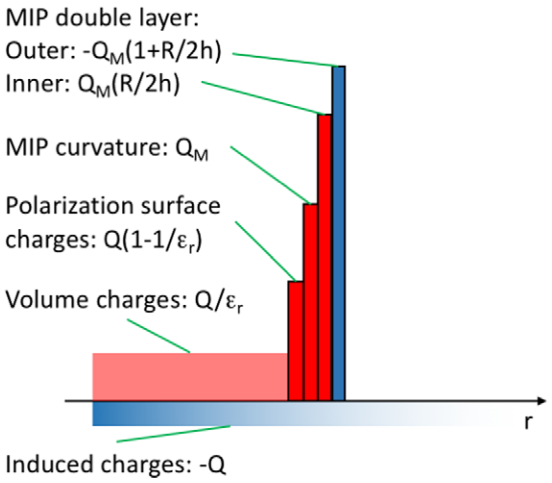

Figure 4. Schematic diagram showing the contributions to the total effective charge density on a dielectric sphere adjacent to a grounded plane. See text for details.

Therefore, the total projected physical charge distribution can be written in the form

$$\sigma_p(r)=\frac{\rho_0}{\epsilon_r}t_p(r)\Theta(R-r)+\frac{4\sigma_{\mathrm{pol}}R}{t_p(r)}\Theta(R-r)+\sigma_i(r), \tag{31}$$

which is shown in figure 5 for both a floating (or laterally supported, as in figure 2(b)) and a supported (as in figure 2(a)) sphere for several values of the relative dielectric constant. Figure 5 illustrates how surface polarization charges, which appear whenever $\epsilon_r>1$, manifest themselves as a bright ring over the circumference that tends to overwhelm the projected volume charge.

4.3. Partial charge measurement in the absence of the MIP contribution

Setting aside temporarily the influence of the MIP on the measurement, we first address the question of how much charge is obtained if the Laplacian of the phase is integrated over only part of the object. We initially consider a rectangular integration domain that extends over the intervals $(-L, x_0)$ along x and $(-L, L)$ along y, where it is assumed that $L\gg R$, as shown schematically in figure 6(a). The fraction of the total charge that is contained within the integration domain is then

$$\begin{aligned}\frac{Q(x_0)}{Q}&=\frac{1}{Q}\int_{-L}^{x_0}\mathrm{d}x\int_{-L}^{L}\mathrm{d}y\,\sigma(\sqrt{x^2+y^2})\\&=\frac{(R+x_0)}{2R}+\frac{x_0(R^2-x_0^2)}{4\epsilon_r R^3}-\left(\frac{1}{2}+\frac{1}{\pi}\arctan\frac{x_0}{R}\right),\end{aligned} \tag{32}$$

where $-R<x_0<R$. In equation (32), the first term (which is linear in x_0) represents a pure surface charge distribution, the second term captures the charge redistribution between the volume and the surface that occurs as a result of polarization and the third term describes the induced charge on the support (if one is present).

Figure 6(b) shows plots of $Q(x_0)/Q$ for both a floating and a supported sphere for $\epsilon_r=1$ (only volume charges) and $\epsilon_r=100$ (only surface charges).

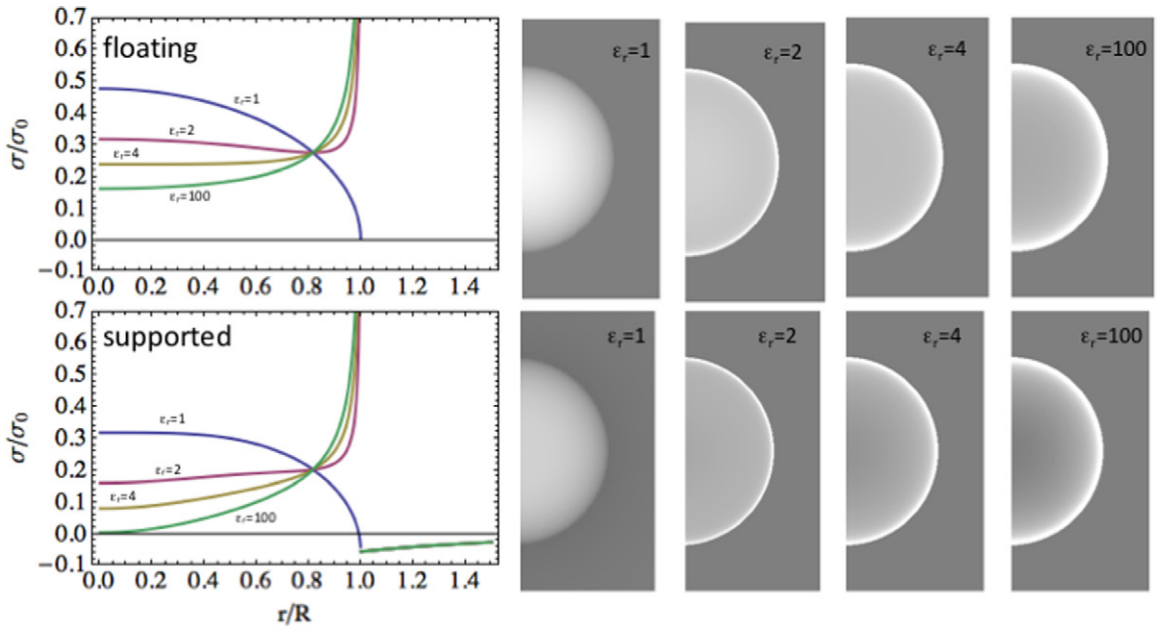

Figure 5. Calculations of the projected charge distribution for a dielectric sphere that is either floating (top) or supported (bottom) for four values of ϵ_r. See text for details.

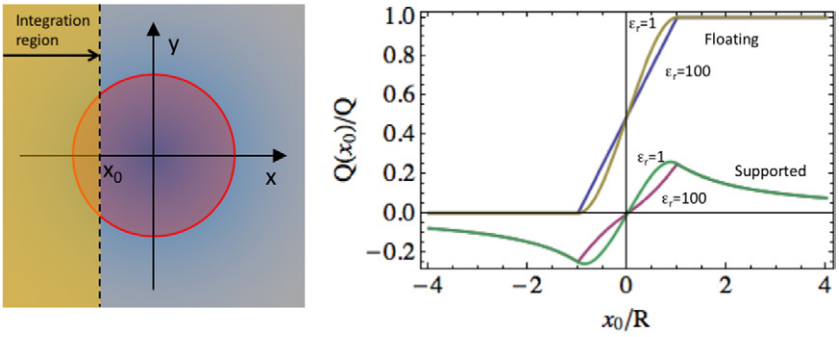

Figure 6. Calculation of the charge that would be measured if the Laplacian of the phase were integrated over only part of a floating or supported dielectric sphere for $\epsilon_r = 1$ and $\epsilon_r = 100$, for a rectangular integration domain that extends over the intervals $(-L, x_0)$ along x and $(-L, L)$ along y where $L \gg R$.

If the integration domain is changed to a concentric circle of radius r_0, then

$$\frac{Q(r_0)}{Q} = \frac{2\pi}{Q}\int_0^{r_0} r\mathrm{d}r\,\sigma(r) = 1 - \sqrt{R^2 - r_0^2}\left(\frac{1}{R} - \frac{r_0^2}{\epsilon_r R^3}\right) - \left(1 - \frac{R}{\sqrt{R^2 + r_0^2}}\right), \tag{33}$$

as shown in figure 7. The relatively large difference between the $\epsilon_r = 1$ and $\epsilon_r = 100$ curves suggests that it may be possible to estimate the dielectric constant of the material by examining the trend of the fractional charge curve in detail. In fact, as $r_0 \to 0$, $Q(r_0)/Q$ becomes quadratic in r_0:

$$\frac{Q(r_0 \to 0)}{Q} \sim \left(\frac{1}{2} + \frac{1}{\epsilon_r} - \frac{1}{2}\right)\frac{r_0^2}{R^2}, \tag{34}$$

where the $-1/2$ appears only in the case of the supported sphere. Therefore, an evaluation of the initial curvature of the fractional charge curve would yield either $1/2 + 1/\epsilon_r$ or $1/\epsilon_r$ for the floating and supported particle, respectively.

4.4. The effect of the MIP on partial charge measurement

Projection of the MIP contribution to the charge density in the electron beam direction requires great care, as infinities abound. According to equation (10), the effective MIP contribution to the projected charge density is

$$\sigma_{\mathrm{MIP}}(r) = -\epsilon_0 V_{\mathrm{M}} \nabla_2^2 t_p(r) = -\epsilon_0 V_{\mathrm{M}}\left(t_p''(r) + \frac{t_p'(r)}{r}\right), \tag{35}$$

which is not problematic in the interior ($r < R$), as

$$\sigma_{\mathrm{MIP}}(r) = 2\epsilon_0 V_{\mathrm{M}} \frac{2R^2 - r^2}{(R^2 - r^2)^{3/2}}. \tag{36}$$

According to equation (36), the curvature of the sphere corresponds to a positive charge density $\sigma_{\mathrm{MIP}}(0) = 2\sigma_{\mathrm{M}}$ at its center in projection (with the factor of 2 arising from the fact that electrons pass through the upper and lower interfaces with vacuum). The interior region then appears positively charged overall. The apparent MIP contribution to the charge distributed in the interior is, however, infinite, as

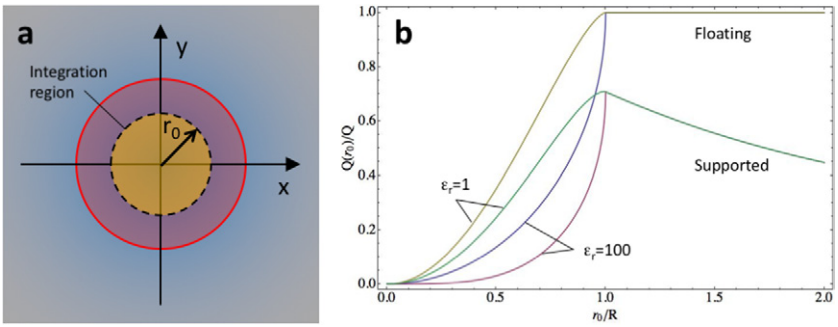

Figure 7. Calculation of the charge that would be measured if the Laplacian of the phase were integrated over only part of a floating or supported dielectric sphere for $\epsilon_r = 1$ and $\epsilon_r = 100$, for a circular integration domain.

$$2\pi \int_0^R \sigma_{\mathrm{MIP}}(r) = \lim_{h\to 0} \frac{Q_{\mathrm{M}}}{2}\sqrt{\frac{R}{2h}}, \tag{37}$$

because of the diverging amount of charge present in the virtual electrodes of the spherical capacitor that represents the MIP potential discontinuity. As discussed above, the charge is compensated by an opposite infinite amount located on the outer layer of the capacitor, but this picture is unsatisfactory.

We now consider three approaches for eliminating the infinities that prevent an assessment of the result of partial charge measurement in the presence of the MIP term: (1) applying a numerical finite difference Laplacian filter to the MIP contribution to the phase shift; (2) working at finite spatial resolution by introducing a point spread function that smooths the phase shift; (3) representing the MIP discontinuity using finite-thickness spherical shells with volume charge densities (i.e. creating a spherical p-n junction).

4.4.1. Numerical Laplacian. Since experimental data always take the form of a digital matrix and differential image algebra involves the use of finite-difference approximations to differential operators, it makes sense to analyze how the MIP contribution to the effective projected charge density appears when the Laplacian of the phase is evaluated numerically. If the MIP contribution to the phase shift $\varphi_{\mathrm{MIP}}(r) = C_{\mathrm{E}} V_{\mathrm{M}} t_p(r)$ is sampled on a square grid with pixel size $h \ll R$, then in the interior region ($r < R$), where $\varphi_{\mathrm{MIP}}(r)$ is continuous and differentiable, the numerical Laplacian works very well and, when rescaled by the factor $-\epsilon_0/C_{\mathrm{E}}$, reproduces equation (36) if the sampling is adequate. However, as r approaches R, the slope of $\varphi_{\mathrm{MIP}}(r)$ increases in magnitude, eventually diverging as $\lim_{r->R^-} \varphi'_{\mathrm{MIP}}(r) = -\infty$. Focusing on the four pixels across $r = R$, i.e. $r = [R-2h, R-h, R, R+h]$ where the projected specimen thickness has values of $[\sqrt{16Rh}, \sqrt{8Rh}, 0, 0]$ to first order in h/R, respectively, the finite-difference Laplacian of the projected thickness

$$t''_p(r) + \frac{t'_p(r)}{r} \sim \lim_{h\to 0} \frac{t_p(r+h) + t_p(r-h) - 2t_p(r)}{h^2} + \frac{t_p(r+h) - t_p(r-h)}{2hr} \tag{38}$$

yields the values $\sqrt{8R}\,[-0.096, -0.58, 1, 0]h^{-3/2}$ in the four pixels. The dipole layer is then captured by the numerical Laplacian as a very large negative charge density at the $r = R$ pixel with value $-\sqrt{2}\,(R/h)^{3/2}\sigma_{\mathrm{M}}$, surrounding a positive charge density at the $r = R - h$ pixel with a value that is approximately 40% smaller. As discussed earlier, the negative layer has to compensate for the positive layer, as well as the apparent charge present in the interior due to the curvature of the object.

4.4.2. Finite-spatial-resolution Laplacian. The easiest way to account for a signal that has finite spatial resolution is to convolve it with a normalized Gaussian point spread function. Evaluation of the convolution and then the Laplacian operation in Fourier space results in the expression

$$\sigma^{\mathrm{FR}}_{\mathrm{MIP}}(r, r_s) = \sigma_{\mathrm{M}} \int_0^\infty q^2 j_1(q) J_0(qr/R) \exp\left(-\frac{q^2 r_s^2}{2R^2}\right) \mathrm{d}q, \tag{39}$$

where $j_1(x)$ is a spherical Bessel function of the first kind and $J_0(x)$ is a Bessel function of the first kind. Setting $r_s = h/\sqrt{2\pi} \sim 0.4\,h$ ensures that the area under the point spread function equals the pixel size squared. With this choice, $\sigma^{\mathrm{FR}}_{\mathrm{MIP}}$ appears as a smoothed version of the numerical Laplacian.

4.4.3. Spherical p-n junction Laplacian. A charge distribution of the form

$$\begin{aligned} \rho^{\mathrm{pn}}_{\mathrm{MIP}}(r) &= 0 && r < R_1 \\ &= +\rho_{\mathrm{pn}} && R_1 < r < R \\ &= -\rho_{\mathrm{pn}} && R < r < R_2 \\ &= 0 && r > R_2, \end{aligned} \tag{40}$$

where $\rho_{\mathrm{pn}} = 2\epsilon_0 V_{\mathrm{M}}/(2R^2 - R_1^2 - R_2^2)$ and R_2 is chosen so as to satisfy the relation $2R^3 - R_1^3 - R_2^3 = 0$, results in a step in MIP that has a magnitude of V_{M} between the $r < R_1$ and $r > R_2$ regions and is connected smoothly by a cubic spline in the $R_1 < r < R_2$ 'depletion region'.

Projection of $\rho^{\mathrm{pn}}_{\mathrm{MIP}}(r)$ then yields the expression

$$\begin{aligned} \frac{\sigma^{\mathrm{pn}}_{\mathrm{MIP}}(r)}{2\rho_{\mathrm{pn}}} &= 2\sqrt{R^2 - r^2} - \sqrt{R_1^2 - r^2} - \sqrt{R_2^2 - r^2} && r < R_1 \\ &= 2\sqrt{R^2 - r^2} - \sqrt{R_2^2 - r^2} && R_1 < r < R \\ &= -\sqrt{R_2^2 - r^2} && R < r < R_2 \\ &= 0 && r > R_2. \end{aligned} \tag{41}$$

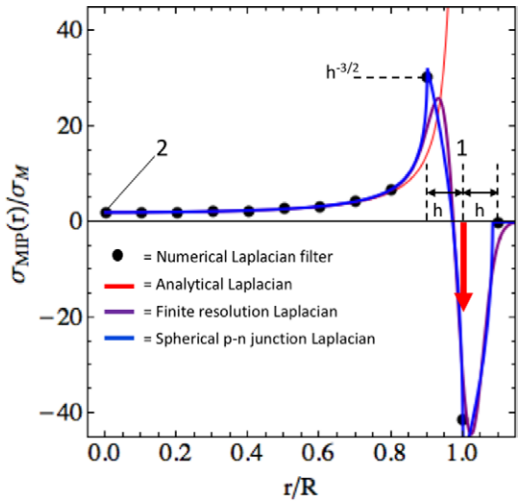

Figure 8. Effective MIP projected charge density according to the analytical model (red curve plus red arrow), numerical Laplacian (black dots), finite-resolution Laplacian (purple curve), spherical p-n junction model (blue curve). The plots are calculated with sampling $h = 0.1\ R$, and are normalized to $\sigma_M = 2\epsilon_0 V_M/R$.

Figure 8 shows the effective projected charge density that appears due to the MIP. The red curve accompanied by the red arrow pointing downwards at $r = R$ represents the analytical expression, equation (36), together with the negatively charged outer layer. The black dots indicate the pixel values of the numerical Laplacian operation with $h = 0.1\ R$ sampling. The sampling might appear relatively coarse (10 pixels on a distance equal to the sphere radius), but it could represent a realistic experimental setup with a $R = 10$ nm sphere sampled with 1 nm pixel size. The purple curve, from equation (39), represents the finite-resolution effective charge density, evaluated for $r_s = 0.04\ R$. The blue curve represents the spherical p-n junction model, from equation (41). All curves overlap almost exactly in the interior, and start to deviate from the analytical expression only two pixels away from the surface. The exterior pixel at $r = R + h$ is zero for the numerical Laplacian and the spherical p-n junction model, and very close to zero for the finite-spatial-resolution Laplacian model. The peak value of the charge density at $r = R - h$ remains finite, but diverges as $h^{-3/2}$ in the limit $h \to 0$. Regardless of the choice of h, the integrated charge in the interior always equals the integrated charge in the exterior, and yields the effective charge density value of $2\sigma_M = 4\epsilon_0 V_M/R$ at $r = 0$.

The MIP contribution to the effective projected charge density $\sigma_{MIP}(r)$ can now be integrated over the rectangular and circular domains used earlier to calculate the apparent charge associated with the MIP. Choosing the finite-spatial-resolution model in the limit $r_s \to 0$ and the rectangular domain for integration yields the expression

$$Q_{MIP}(x) = \int_{-\infty}^{x} \lambda_{MIP}(x')\mathrm{d}x', \tag{42}$$

where

$$\lambda_{MIP}(x) = \sigma_M \int_{-\infty}^{\infty} \mathrm{d}y \int_0^{\infty} q^2 j_1(q) J_0(q\sqrt{x^2+y^2}/R)\mathrm{d}q. \tag{43}$$

Since

$$\int_{-\infty}^{\infty} J_0(q\sqrt{x^2+y^2}/R)\mathrm{d}y = \frac{2R}{q}\cos(q|x|/R), \tag{44}$$

it follows that

$$\lambda_{MIP}(x) = 2R\sigma_M \int_0^{\infty} q j_1(q)\cos(q|x|/R)\mathrm{d}q. \tag{45}$$

By making use of the relation $\cos(x) = j_0(x) - x j_1(x)$, a tabulated integral and the orthogonality of Bessel functions, this expression becomes

$$\lambda_{MIP}(x) = \pi R\sigma_M(\Theta(R-|x|) - R\delta(|x|-R)). \tag{46}$$

Finally, we have the result

$$\frac{Q_{MIP}(x)}{Q_M} = \frac{x_0}{4R}\Theta(R-|x|). \tag{47}$$

According to equations (46) and (47), the effective linear charge density resulting from the integration of $\sigma_{MIP}(r)$ along one axis is a positive constant surrounded by two negative deltas representing the compensating charge on the 'outer electrode' of the spherical capacitor that describes the MIP. Partial charge measurement then gives a linear function in the interior, with finite discontinuities at the edge. The two functions $\lambda_{MIP}(x)$ and $Q_{MIP}(x)$ are plotted on the same graph in figure 9(a).

It is now possible to quantify the influence of the MIP on a partial charge measurement. For simplicity, a floating spherical object with pure surface charge and $Q(x)/Q = (x+R)/(2R)$ (corresponding to the limit $\epsilon_r \to \infty$ in equation (32)) is considered. As shown in figure 9(b), the MIP affects the slope of the partial charge curve, while carrying the two edge discontinuities. As a consequence, as the boundary of the integration domain is moved to intercept spherical caps of increasing height, the object first appears to be negatively charged, then neutral at $x/R = -1/(1 - Q_M/(2Q))$, then by symmetry correctly charged with $Q/2$ at $x = 0$ (corresponding to a half sphere intercepted). Finally, just before sweeping over the entire object, the measurement is overcharged by an amount $+Q_M/2$, but as soon as the integration domain boundary is outside again the measured charge drops back to the expected value of $+Q$.

5. Geometries other than a sphere

5.1. Nanowires and nanotubes

For a nanowire or nanotube, it is not easy to calculate the way in which an initial (e.g. uniform) charge distribution relaxes to accommodate polarization, or how charge redistributes in response to an applied electric field or to boundary conditions. For example, if charge Q is placed on a dielectric wire, a fraction of it is expected to be brought to the surface (both lateral and end caps) as a result of polarization. However, this fraction depends on the length/diameter ratio of the wire, as well as on the shape of its terminations. In the extreme case of a metallic wire, for which charges can only be distributed on the surface of the object in such a way as to make the surface equipotential, the concept of self-capacitance can be used

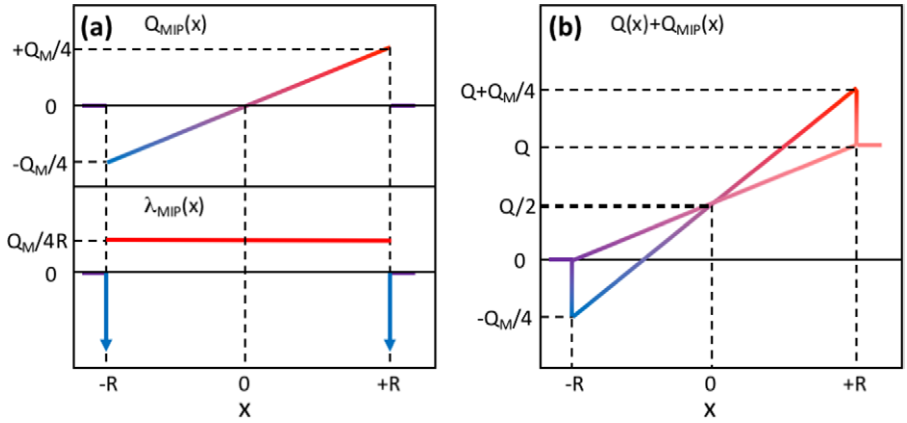

Figure 9. (a) The two functions $\lambda_{\mathrm{MIP}}(x)$ and $Q_{\mathrm{MIP}}(x)$ plotted on the same graph. (b) The influence of the MIP on a partial charge measurement for a floating spherical object with pure surface charge and $Q(x)/Q = (x + R)/(2R)$ (corresponding to the limit $\epsilon_r \to \infty$ in equation (32)). See text for details.

to determine the surface potential. However, this approach does not provide much information about the charge distribution itself. Without being able to model the expected charge distribution properly, it is left unspecified and only the MIP contribution to its measurement in this geometry is considered here.

If x is chosen as the symmetry axis of the cylinder, then the projected thickness $t_p(y) = 2\sqrt{R^2 - y^2}$ does not depend on x. The effective MIP contribution to the charge distribution in the interior $-R < y < R$ is given by the expression

$$\sigma_{\mathrm{MIP}}(y) = -\epsilon_0 V_{\mathrm{M}} t_p''(y) = \epsilon_0 V_{\mathrm{M}} \frac{2R^2}{(R^2 - y^2)^{3/2}}, \qquad (48)$$

which differs from the spherical geometry in that there is no effect of curvature along x. The magnitude of the effective charge density involved is therefore halved. (Compare equations (48) and (36) at $y = 0$ and $r = 0$, respectively).

For a cylinder, the step in MIP can be imagined as the potential of a cylindrical capacitor, where the effective negative charge density on the outer electrode is slightly greater than the positive charge density on the inner electrode (the dipole layer is still asymmetrical, since the object's surface is curved) and the amount of effective charge involved still diverges as the two electrodes approach each other. The (linear) charge density of the negative layer can be represented in projection in the form

$$-2\epsilon_0 V_{\mathrm{M}} R \frac{\delta(|y| - R)}{\sqrt{R^2 - y^2}}, \qquad (49)$$

which is the correct infinite amount needed to compensate the charge density that has moved to the interior.

The positive implication of the lack of curvature along the symmetry axis of the cylinder is that, as long as one boundary of the integration domain cuts through the wire, it is certain that a partial charge measurement corresponds precisely to the amount of charge that is physically present within the domain. This statement validates the experimentally determined charge density profile along a carbon nanotube bundle reported in [23].

5.2. Samples with flat surfaces

For a specimen that has flat top and bottom surfaces, the MIP contribution to the charge density is a symmetrical dipole layer above and below the object (which is invisible when viewed in projection) and similar dipole layers at its edges. Whether the dipoles at the edges are symmetrical or asymmetrical depends on the edge curvature. In the absence of edge curvature, the dipole layer is symmetrical and its effects are absorbed as soon as the integration domain crosses the edge. For an ideal sample that takes the form of a prism with a rectangular cross-section and is oriented with two axes perpendicular to the electron beam direction, the effect of the MIP is confined to the edges of the sample, with no apparent charge brought into the interior region. This is the only conceivable scenario when the Laplacian of the phase is directly and meaningfully interpretable in terms of a physical charge density anywhere in the interior and where integration of the Laplacian over a domain that intercepts a portion S of the projected object yields precisely the amount of charge that is present within the volume St, where t is the specimen thickness in the electron beam direction.

Figure 10 illustrates schematically the MIP charge densities associated with wires of various cross sections. Figure 10(a) represents a wire with rectangular cross section, observed at zero tilt, where the projected thickness is a top-hat function and, therefore, the MIP effective charge is present only where the thickness changes abruptly from t to zero. Figure 10(b) represents the same wire observed with some tilt, where the projected thickness has a trapezoidal shape. In this case, the dipole layer splits into a negative charge line at the position where the thickness starts increasing, and a positive charge line at the position where the thickness stabilizes to the value $t/\cos\alpha$, if α is the tilt angle. In general, for faceted objects with no curvature, a negative charge line forms whenever the thickness gradient increases abruptly, compensated by a positive charge line when the thickness gradient decreases abruptly. Figure 10(c) shows a wire with cylindrical cross section, discussed earlier. The two negative charge lines can be described by equation (49), while the continuous charge density in the interior is captured by equation (48). The effective

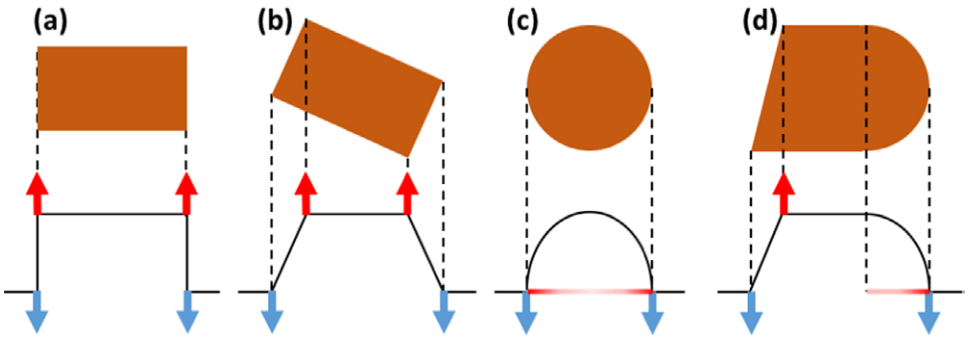

Figure 10. Schematic view of the effective MIP charge densities from wires of various cross sections: (a) rectangular cross section observed with no tilt, (b) rectangular cross section observed with some tilt, (c) circular cross section, (d) composite cross section with a faceted side and a rounded side.

MIP charge density for a hypothetical wire with a cross section that involved a faceted left-hand side and a rounded right-hand side is shown in figure 10(d), and reflects a combination of the previous cases.

In the presence of edge curvature, the dipole layer is asymmetrical and the effect of the MIP has to be taken into account just as for a spherical object, although no effective charge is present in the interior. For example, for an object that has the shape of a disk of radius R and thickness t, the MIP contribution to the projected effective charge density is

$$\sigma_{\mathrm{MIP}}(r) = -\epsilon_0 V_{\mathrm{M}} t \nabla_2^2 \Theta(R-r) = \epsilon_0 V_{\mathrm{M}} t \left(\frac{\delta(r-R)}{r} + \delta'(r-R) \right), \quad (50)$$

which is confined to the edge and brings no effective charge into the interior. For a circular integration domain of radius r_c, the MIP is invisible, as

$$\int_0^{r_c} r \left(\frac{\delta(r-R)}{r} + \delta'(r-R) \right) \mathrm{d}r = 0 \quad (51)$$

equally for $r_c < R$ (where both integrands are zero) and $r_c > R$ (where the $\delta(x)$ and $\delta'(x)$ terms are 1 and -1, respectively).

If, instead, the integration domain is rectangular, then the asymmetry of the dipole layer manifests itself as soon as a projection is taken along one direction. Then,

$$\begin{aligned} \lambda_{\mathrm{MIP}}(x) &= \int_{-\infty}^{\infty} \sigma_{\mathrm{MIP}}(\sqrt{x^2+y^2})\mathrm{d}y \\ &= 2\epsilon_0 V_{\mathrm{M}} t \left(\frac{R^2}{(R^2-x^2)^{3/2}} - \lim_{h\to 0} \sqrt{\frac{R}{2h}} \left(\delta(x+R) + \delta(x-R)\right) \right), \end{aligned} \quad (52)$$

leading to an apparent cumulative charge of

$$Q_{\mathrm{MIP}}(x) = \int_{-\infty}^{x} \lambda_{\mathrm{MIP}}(x')\mathrm{d}x' = 4\epsilon_0 V_{\mathrm{M}} t \frac{x}{\sqrt{R^2-x^2}} \quad (53)$$

for $|x| < R$, while $Q_{\mathrm{MIP}}(x) = 0$ for $|x| > R$. Whereas the magnitude of the MIP contribution to the partial charge measurement on a disk is proportional to the t/R aspect ratio, which is generally small, the apparent charge displacement is particularly strong at the edge of the disk, where $Q_{\mathrm{MIP}}(x)$ diverges.

Figure 11 shows results obtained from a numerical test carried out on a $t = 10\,\mathrm{nm}$, $R = 10\,\mathrm{nm}$ disk, which is charged uniformly with $100\,|e|$ and has a MIP V_{M} of 10 V. The phase shown in figure 11(a) was sampled over a 128×128 pixel square grid (with a pixel size p of 0.39 nm). A normally-distributed noise pattern (with a standard deviation $\Delta\varphi$ of 63 mrad) was superimposed onto the phase image. The Laplacian of the phase, which is shown in figure 11(b), is dominated by the dipole layer associated with the MIP, which overwhelms the mean intensity change between the interior and exterior, as expected. The noise level in the Laplacian of the phase is 1.83 rad nm^{-2} (standard deviation), which is precisely $\sqrt{20}$ times the phase noise divided by the pixel size squared. This is due to the numerical filter operating by adding the values of the four pixels on the left, on the right, above and below the target pixel (i, j), and subtracting from it four times the value of the target pixel itself. Since noise adds in quadrature, the Laplacian of a noisy image with unit standard deviation will have $\sqrt{4 \times 1^2 + 4^2} = \sqrt{20}$ standard deviation.

When it is converted into a charge density by incorporating the factor $-\epsilon_0/C_{\mathrm{E}}$, the noise corresponds to fluctuations in the measured charge density of approximately 15 e nm^{-2}, or 2.4 e pixel^{-1}. This value is much greater than the physical charge density present of 0.3 e nm^{-2}. Although great care is therefore needed when interpreting charge density maps derived from the Laplacian of the phase, a positive aspect of such measurements is that the noise in the Laplacian of the phase has a mean value of zero and so, to an extent, can be 'integrated away'. This point is illustrated in figure 11(c), in which the cumulative charge $Q(x)$ obtained by integrating the Laplacian of the phase over the expanding rectangular domain sketched in figure 11(b) is plotted in yellow. The purple curve in figure 11(c) shows the MIP contribution to the charge profile derived from a noise-free phase image, which exhibits oscillations that are comparable to the noise as a result of the mismatch between the circular edge and the square grid employed for sampling. This mismatch is a numerical artefact that is equivalent to an edge roughness of the order of the pixel size, and is highlighted in figure 11(b).

For a rectangular contour of $N \times M$ pixels, the integrated noise yields a random number at every pixel, which is distributed normally about zero with a standard deviation of $\Delta Q = (2\sqrt{N+M-2})\epsilon_0 \Delta\varphi / C_{\mathrm{E}}$. In the example considered here, this value corresponds to a fluctuation in the cumulative charge curve ranging from approximately 12 electrons on

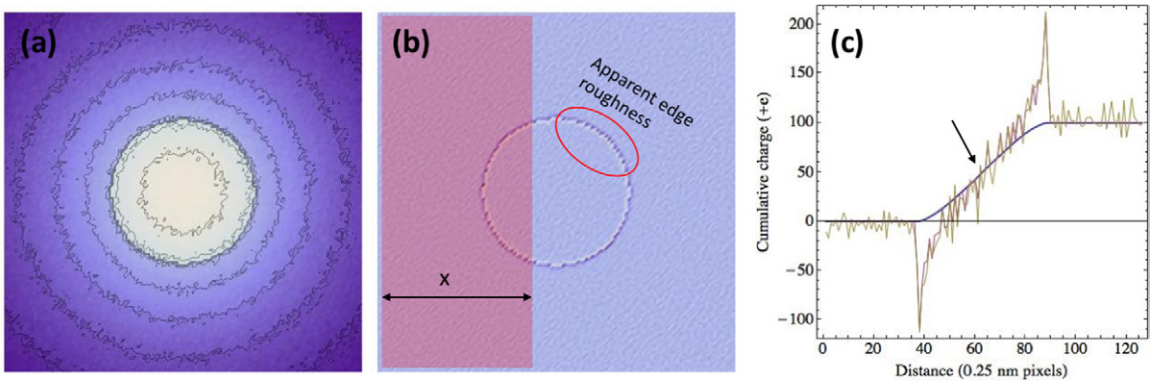

Figure 11. (a) Phase image calculated for a $t = 10\,\text{nm}$, $R = 10\,\text{nm}$ disk, which is charged uniformly with $100\,|e|$ and has a MIP of 10 V. The image is sampled over a 128×128 pixel square grid with a pixel size p of 0.39 nm and with normally-distributed noise superimposed onto it. The phase image is plotted over the range $(-3.4, 0.8)$ rad, and the phase contours are drawn every 0.5 rad. (b) Laplacian of the phase, which is dominated by the dipole layer associated with the MIP. The semi-transparent purple rectangle denotes one of the integration domains, 55 pixels wide, which yields the cumulative charge value indicated by an arrow in (c). (c) Cumulative charge curves obtained by integrating the Laplacian of the phase over the expanding rectangular domain sketched in (b). The blue curve is the expected cumulative charge in absence of noise and MIP; the purple curve represents the expected cumulative charge from the noise-free image; the yellow curve is the cumulative charge measured from the noisy phase image shown in (a).

the left side of the object to approximately 17 electrons on the right side. The noise fluctuations increase with the size of the integration domain because the procedure does not simply involve averaging, but adds statistically independent random pixel values. It therefore appears to be advantageous to use integration domains that are as small as the size of the object allows. However, if the cumulative charge curve could be fitted with a constant, for example in the vacuum area on the right side of the object, then one would effectively average the curve, thereby removing the dependency of ΔQ on the number of pixels.

6. Experimental results

A sample suitable for studies of electron beam induced charging was fabricated using focused ion beam (FIB) milling. A FIB-milled lamella of sapphire was initially welded onto a Cu grid. Two trenches were then cut at opposite sides of it until a tip-like shape was obtained. An off-axis electron hologram and a vacuum reference electron hologram were recorded at 300 kV on an FEI Titan TEM using a holographic interference fringe spacing of 2 nm (resulting in a spatial resolution in reconstructed phase images of approximately 6 nm). The complex exit wave was reconstructed from each recorded electron hologram using a standard Fourier-transform-based algorithm.

A representative experimental phase image of the sapphire tip is shown in figure 12(a). The image is sampled on a 128×128 pixel grid with a pixel size of 3.5 nm. The presence of a phase contour in vacuum immediately suggests that the tip has been charged by the electron beam. This observation is confirmed by the presence of a slope in vacuum in line profiles generated from the phase image, which are shown in figure 12(b). The change in slope in vacuum on each side of the green profile confirms that the tip is charged, while the sense of the change in slope confirms that it is charged positively. The slight difference in slope on each side of the tip is likely to originate from perturbation of the reference wave [6], although it may also be affected by non-uniformity of the object's charge density. The phase image and the line profiles reveal that the tip has an irregular shape, with an almost flat side (perhaps a facet) oriented in the electron beam direction at its upper edge, a rounded end and a wedge-shaped lower edge.

Without a knowledge of the MIP contribution to the phase and of the perturbation of the vacuum reference wave, it is impossible to relate the details of the internal and external phase contours to the charge distribution and the only unequivocal determination that can initially be made is that the tip is charged.

However, the Laplacian of the phase image, which is shown in figure 13(a), provides more information about the charge in the tip. Feature A takes the form of two almost overlapping dipole layers, which are likely to correspond to the projected thickness changing abruptly twice, perhaps at a two-step terrace. This observation is consistent with the green phase profile shown in figure 12(b) at a position of approximately 300 nm. Feature B, where the dipole layer is well separated into negative and positive charged lines, is a clear fingerprint of a wedge, in which the thickness increases linearly with distance with little or no curvature. See also figure 10(b). Feature C highlights a region where a distinct positively charged arc fades away, with a clear negatively charged line following the curved edge of the tip. This behavior suggests that the apex may have an additional small protrusion, similar to a small spherical cap attached to a more faceted terminating region. Another possibility is that feature C is related to physical charge accumulating at the apex. Without a knowledge of the MIP contribution to the phase shift, it is not possible to discriminate between these two hypotheses.

Figure 13(b) shows a cumulative charge curve, which is generated from the region marked in figure 13(a) and illustrates how dominant the MIP contribution to the charge profile can be. Without considering the effect of the MIP, it would be

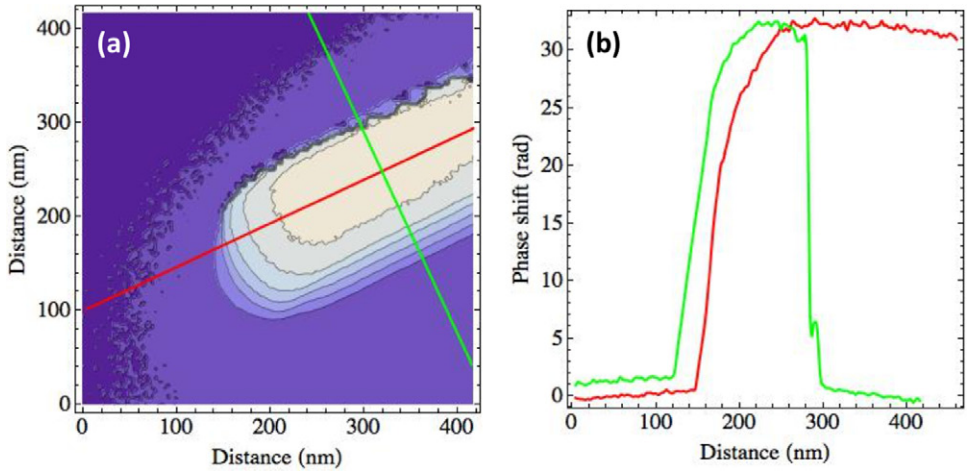

Figure 12. (a) Representative experimental electron holographic phase image recorded from a sapphire tip, sampled on a 128×128 pixel grid with a pixel size of 3.5 nm; phase contours are spaced by 5 rad. (b) Phase profiles extracted along the lines shown in (a).

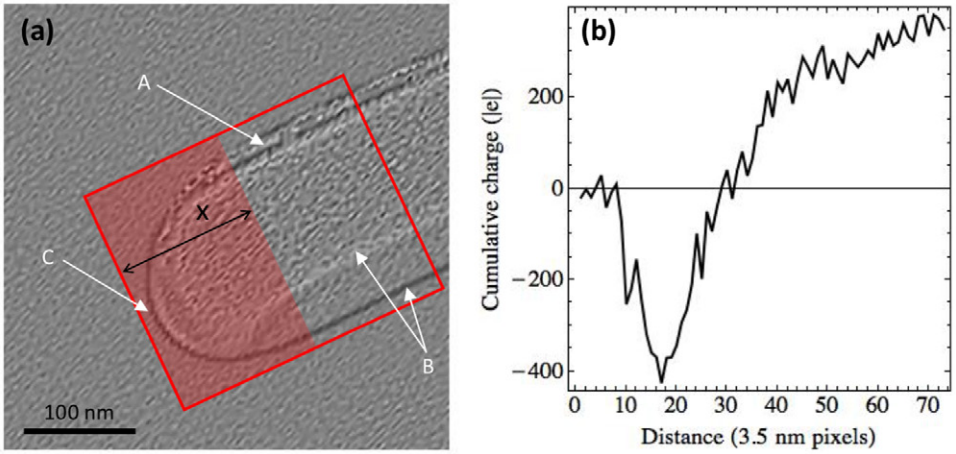

Figure 13. (a) Laplacian of the phase image shown in figure 12(a), with the rectangular region of integration marked as a red line; the integration domain for each partial charge measurement is indicated by the semi-transparent rectangle of width x, and spans the integration region from left to right. (b) Cumulative charge curve obtained as a set of partial charge measurements over rectangular domains of width x (see (a)), for $0 < x < 255$ nm.

possible to conclude that the tip is *negatively* charged until about 70 nm from its end and then only becomes positively charged afterwards. Instead, for the present sample morphology, before the cumulative charge profile begins to reflect the presence of physical charges it is also affected by the presence of edges and curved portions of the sample, even though the contribution from the MIP is charge-neutral overall. This transition, where the curve stabilizes to a constant value, occurs approximately 160 nm from the end of the tip, or approximately 50 nm from the apparent 'charge-neutrality' position.

Linear interpolation suggests that the tip interior is associated with a constant charge density of approximately 1.53 e nm^{-1}. If the cross-section of the tip is treated as a circle of radius 100 nm, then this value corresponds to either a surface charge density of approximately 2400 e μm^{-2}, or a volume charge density of approximately 50 000 e μm^{-3}, or a combination of the two, depending on the dielectric constant of the material (which cannot be estimated from this dataset). Regardless of the value of ϵ_r, the electric field that is generated in vacuum by a cylindrical wire that has a linear charge density of 1.53 e nm^{-1} is approximately 44 mV nm^{-1}. The measured charge density is low, but well above the noise level and clearly detectable.

7. The effect of magnetic perturbations

An illustration of a final possible source of error is provided by the fact that if a spherical object is magnetized uniformly with saturation magnetization M_S, in addition to being charged by an amount Q, then it will have both a uniform surface distribution of electrical charge $\sigma_0 = Q/(4\pi R^2)$ and a dipolar surface distribution of magnetic charge $\sigma_{mag} = M_S \cos\theta$. If it is not known that the object is magnetic and the Laplacian of the phase is calculated by multiplying it by the factor $-\epsilon_0/C_E$ that is needed to convert it into a charge density, then the apparent charge density is

$$\frac{4R}{t_p(r)}\left(\sigma_0 + \frac{\pi}{C_E \phi_0 c^2}\frac{x}{R}M_S\right), \tag{54}$$

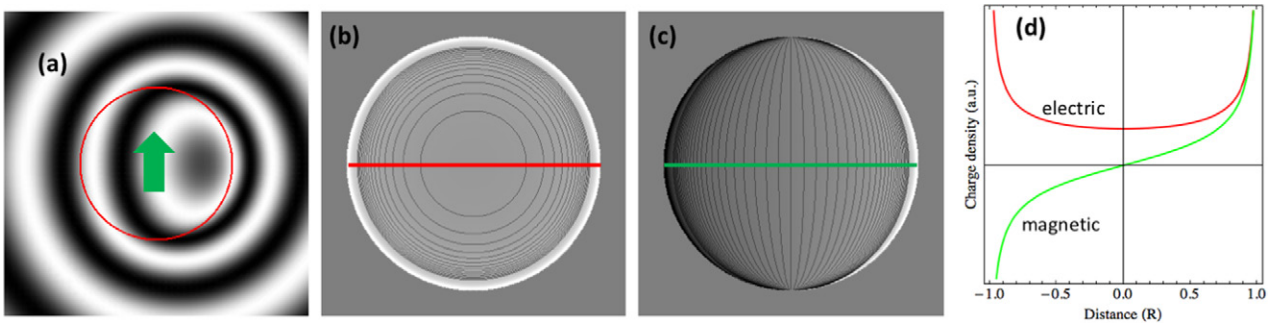

Figure 14. (a) Phase image, 128 × amplified, calculated by adding the electrostatic phase shift from $Q = 10|e|$ of charge and the magnetic phase shift from $M_S = 480$ kA m^{-1} of magnetization for a $R = 10$ nm sphere. The mean inner potential contribution to the phase shift is neglected in this example. (b) Projected electric charge density, (c) projected magnetic charge density, and (d) their profiles across the diameter perpendicular to the direction of the magnetization.

where $\phi_0 = h/2e = 2.07 \times 10^{-15}$ T m^2 is the flux quantum and c is the speed of light. The factor $\pi/C_E\phi_0 c^2$ has units of inverse velocity and is equal to 2.58 ns m^{-1} at 300 kV. In fact, considering that $C_E = e/\hbar\beta c$, it can also be written very simply as $\beta/c = v/c^2$, where v is the velocity of the beam electrons. For a typical value of M_S of 480 kA m^{-1} (for magnetite), the effective charge density is 1.2 mC m^{-2} or 0.008 e nm^{-2}. For comparison, the same charge density results from the presence of 10 electrons of charge distributed over the surface of a non-magnetic sphere with $R = 10$ nm.

Another comparison can be made by considering a spherical particle that carries a single flux quantum. If $\pi R^2 \mu_0 M_S = \phi_0$, then the equivalent charge is β/α electrons, where α is the fine structure constant. In this very special context, the presence of one flux quantum is equivalent to approximately 137 electrons at a high enough accelerating voltage (i.e. when $\beta \to 1$).

Figure 14(a) shows the phase image, 128 × amplified, corresponding to a $R = 10$, $\epsilon_r = 100$ dielectric sphere charged with $Q = 10|e|$ and magnetized at $M_S = 480$ kA m^{-1} along the direction indicated by the green arrow. The magnetization breaks the circular symmetry of the phase image, which could be misinterpreted as charge accumulation towards the right-hand side of the image, or, equivalently, as a net electrical polarization of the dielectric object towards the right. The phase Laplacian converted into charge density is shown in figure 14(b) for the electrostatic phase shift, and in figure 14(c) for the magnetic phase shift. Their diametral profiles are shown in figure 14(d), and illustrate how, in this example, the two charge densities have a similar magnitude.

8. Conclusions

The factors that influence the measurement of the local charge inside a specimen in the transmission electron microscope from the Laplacian of the electron-optical phase measured using off-axis electron holography have been presented and discussed. It has been shown that the approach can be reliable for determining the total charge in an object of interest. However, care is required when the integration boundary spans only part of the object, both as a result of the presence of an apparent surface charge density arising from the mean inner potential and specimen thickness profile and as a result of induced charges in nearby substrates and electrodes. The influence of noise and magnetization on the measured charge density was also discussed.

Acknowledgments

We acknowledge financial support from the European Union under the Seventh Framework Programme under a contract for an Integrated Infrastructure Initiative (Reference 312483 ESTEEM2). The research leading to these results has received funding from the European Research Council under the European Union's Seventh Framework Programme (FP7/2007-2013)/ ERC grant agreement number 320832.

References

[1] Tonomura A 1999 *Electron Holography* (*Springer Series in Optical Science*) 2nd edn (New York: Springer)
[2] Dunin-Borkowski R E, McCartney M R and Smith D J 2004 Electron holography of nanostructured materials *Encyclopedia of Nanoscience and Nanotechnology* vol 3, ed H Nalwa (Stevenson Ranch, CA: American Scientific) pp 41–100
[3] McCartney M R and Smith D J 2007 *Annu. Rev. Mater. Res.* **37** 729–67
[4] Lichte H and Lehmann M 2008 *Rep. Prog. Phys.* **71** 016102
[5] Völkl E, Allard L F and Joy D C (ed) 2013 *Introduction to Electron Holography* (New York: Springer)
[6] Matteucci G, Missiroli G F, Nichelatti E, Migliori A, Vanzi M and Pozzi G 1991 *J. Appl. Phys.* **69** 1835–42
[7] Matteucci G, Missiroli G F and Pozzi G 2002 Electron holography of long-range electrostatic fields *Advances in Imaging and Electron Physics* vol 122, ed P W Hawkes (Amsterdam: Elsevier) pp 173–249
[8] Frabboni S, Matteucci G, Pozzi G and Vanzi M 1985 *Phys. Rev. Lett.* **55** 2196
[9] Rau W, Schwander P, Baumann F, Höppner W and Ourmazd A 1999 *Phys. Rev. Lett.* **82** 2614
[10] Gribelyuk M, McCartney M, Li J, Murthy C, Ronsheim P, Doris B, McMurray J, Hegde S and Smith D J 2002 *Phys. Rev. Lett.* **89** 025502
[11] Cooper D, Ailliot C, Barnes J P, Hartmann J M, Salles P, Benassayag G and Dunin-Borkowski R E 2010 *Ultramicroscopy* **110** 383–9
[12] Twitchett-Harrison A C, Yates T J, Newcomb S B, Dunin-Borkowski R E and Midgley P A 2007 *Nano Lett.* **7** 2020–3

[13] Wolf D, Lubk A, Lenk A, Sturm S and Lichte H 2013 *Appl. Phys. Lett.* **103** 264104
[14] Frost B and Völkl E 1999 *Mater. Charact.* **42** 221–7
[15] Lloyd S, Dunin-Borkowski R and Boothroyd C 1997 *Inst. Phys. Conf. Ser.* **153** 113–6
[16] McCartney M, Gribelyuk M, Li J, Ronsheim P, McMurray J and Smith D J 2002 *Appl. Phys. Lett.* **80** 3213–5
[17] Downing K H, McCartney M and Glaeser R M 2004 *Microsc. Microanal.* **10** 783–9
[18] Dunin-Borkowski R E, Newcomb S B, Kasama T, McCartney M R, Weyland M and Midgley P A 2005 *Ultramicroscopy* **103** 67–81
[19] Gajdardziska-Josifovska M, McCartney M, De Ruijter W, Smith D J, Weiss J and Zuo J 1993 *Ultramicroscopy* **50** 285–99
[20] Li J, McCartney M, Dunin-Borkowski R and Smith D J 1999 *Acta Crystallogr.* A **55** 652–8
[21] Kruse P, Schowalter M, Lamoen D, Rosenauer A and Gerthsen D 2006 *Ultramicroscopy* **106** 105–13
[22] Cumings J, Zettl A, McCartney M and Spence J 2002 *Phys. Rev. Lett.* **88** 056804
[23] Beleggia M, Kasama T, Dunin-Borkowski R E, Hofmann S and Pozzi G 2011 *Appl. Phys. Lett.* **98** 243101
[24] Matteucci G, Missiroli G F, Muccini M and Pozzi G 1992 *Ultramicroscopy* **45** 77–83
[25] Kim J J, Shindo D, Murakami Y, Xia W, Chou L J and Chueh Y L 2007 *Nano Lett.* **7** 2243–7
[26] Beleggia M, Kasama T, Larson D, Kelly T, Dunin-Borkowski R and Pozzi G 2014 *J. Appl. Phys.* **116** 024305
[27] Migunov V, London A, Farle M and Dunin-Borkowski R E 2015 *J. Appl. Phys.* **117** 134301
[28] Mildner S, Beleggia M, Mierwaldt D, Hansen T W, Wagner J B, Yazdi S, Kasama T, Ciston J, Zhu Y and Jooss C 2015 *J. Phys. Chem.* C **119** 5301–10
[29] Matteucci G, Medina F and Pozzi G 1992 *Ultramicroscopy* **41** 255–68
[30] Pozzi G, Beleggia M, Kasama T and Dunin-Borkowski R E 2014 *C. R. Phys.* **15** 126–39
[31] Wolf D, Lubk A, Röder F and Lichte H 2013 *Curr. Opin. Solid State Mater. Sci.* **17** 126–34
[32] Lubk A, Wolf D, Simon P, Wang C, Sturm S and Felser C 2014 *Appl. Phys. Lett.* **105** 173110
[33] Rodenburg J 2008 *Adv. Imaging Electron Phys.* **150** 87–184
[34] Gureyev T E and Nugent K A 1997 *Opt. Commun.* **133** 339–46
[35] Petersen T C, Keast V J and Paganin D M 2008 *Ultramicroscopy* **108** 805–15
[36] Merli P, Missiroli G and Pozzi G 1975 *Physica Status Solidi* a **30** 699–711
[37] Beleggia M, Capelli R and Pozzi G 2000 *Phil. Mag.* B **80** 1071–82
[38] Dekkers N and De Lang H 1974 *Optik* **41** 452–6
[39] Lohr M, Schregle R, Jetter M, Wächter C, Wunderer T, Scholz F and Zweck J 2012 *Ultramicroscopy* **117** 7–14
[40] Lubk A and Zweck J 2015 *Phys. Rev.* A **91** 023805
[41] Gatel C, Lubk A, Pozzi G, Snoeck E and Hÿtch M 2013 *Phys. Rev. Lett.* **111** 025501
[42] Beleggia M and Pozzi G 2010 *Ultramicroscopy* **110** 418–24
[43] O'Keeffe M and Spence J 1994 *Acta Crystallogr.* A **50** 33–45
[44] Pennington R S, Boothroyd C B and Dunin-Borkowski R E 2015 *Ultramicroscopy* **159** 34–45